RSC Advances

ROYAL SOCIETY OF CHEMISTRY

www.rsc.org/advances

SiO_2–$Ti_{0.98}In_{0.01}Nb_{0.01}O_2$ composite ceramics with low dielectric loss, high dielectric permittivity and enhanced breakdown electric field

JingleiLi[a], ZhuoXu[a], FeiLi[a*], Xuhui Zhu[a], and ShujunZhang[b]

SiO_2–$Ti_{0.98}In_{0.01}Nb_{0.01}O_2$ (SiO_2–TINO) composite ceramics were synthesized by solid-state sintering methods. The dielectric loss can be lowered and the breakdown electric field can be greatly enhanced by doping 2 mol% SiO_2 into TINO ceramics, while preserving the relatively high dielectric permittivity (~30000). The microstructure and electrical response of SiO_2–TINO composite ceramics were studied to investigate the reasons for these good dielectric properties. The lower dielectric loss and enhanced breakdown electric field were attributed to the embedding of SiO_2 in the TINO grain boundaries, which induced a drop in potential and a blocking effect around the grain boundaries for the 2 mol% SiO_2–TINO composite ceramic. The results provide a way to lower the dielectric loss and enhance the breakdown voltage by tuning of the grain boundary.

[a.] *Electronic Materials Research Laboratory, Key Laboratory of the Ministry of Education and International Centre for Dielectric Research, Xi'an Jiaotong University, Xi'an 710049, China.E-mail: ful5@mail.xjtu.edu.cn*

[b.] *Materials Research Institute, Pennsylvania State University, University Park, Pennsylvania 16802, USA.*

Introduction

Materials with colossal permittivity (CP, i.e., a relative dielectric permittivity larger than 1000) are of focal interest because of their potential use in smaller and faster electronics. Recently, remarkable dielectric behavior has been reported in (Nb+In) co-doped TiO_2 (TINO) ceramics,[1] which possessed colossal dielectric permittivity (>10^4) over a wide temperature range from 80 to 450 K and show potential to replace state-of-the-art CP materials, such as $CaCu_3Ti_4O_{12}$[2] and doped-$BaTiO_3$.[3]

However, the dielectric loss was found to be susceptible to the sintering schedule (i.e., heating rate, cooling rate, sintering temperature, holding time, and sintering atmosphere), and the breakdown electric field was quite low for TINO ceramics. These disadvantages may inhibit further application of these ceramics.[1b,1g] Thus, decreasing the dielectric loss and enhancing the breakdown electric field is important for TINO ceramics. Although the origin of the colossal dielectric permittivity is still an open question[1], the conductivity of the grain boundary was thought to play an important role in the high dielectric loss of TINO ceramics.[1c,1g] From the methods employed in other CP ceramics (adding $CaTiO_3$[4],La_2O_3[5], ZrO_2[6], NiO[7], Al_2O_3[8], SiO_2[9], and MnO[10] to decrease dielectric loss), we chose SiO_2 to dope into TINO ceramics to achieve a low dielectric loss and high breakdown electric field, because SiO_2 possesses large band-gap energy and high resistance. The results demonstrated that the secondary SiO_2 phase that aggregated around the grain

boundaries could decrease the dielectric loss and enhance the breakdown electric field; meanwhile, a high dielectric permittivity of ~30000 was preserved.

Results and Discussion

Fig. 1a shows the XRD powder patterns for SiO_2–TINO composite ceramics, where the XRD peaks of rutile TiO_2, anatase TiO_2, and cristobalite SiO_2 are also shown to confirm the phase structure of prepared ceramics. The lattice planes of the rutile phase are given according to the XRD card. The XRD patterns showed that a second phase of SiO_2 and a minor anatase phase existed in all SiO_2–TINO ceramics. The inset of Fig. 1a shows the shift of the (101) plane peak with increasing SiO_2, indicating the change of the lattice parameters of TiO_2. The lattice parameters (a, c) exhibited a maximum value when the TINO ceramics were doped with 2 mol% SiO_2, dropping remarkably with the addition of SiO_2; however, a slight increase appeared at a high doping level (> 6mol%), as shown in Fig. 1b. The change of the lattice parameter was thought to be induced by the SiO_2 phase transition during the cooling stage and not by diffusion of Si(IV) cations, leading to an internal stress/strain of the grains. As the Ti(radius 0.605 Å[13]) occupy the center site to form [TiO_6] octahedrons, Si(IV) (radius 0.4 Å[13]) occupy the center site to form [SiO_4] tetrahedrons. According to solid solution law, |0.605-0.4/0.605|=34% is much higher than the infinite solid solution's upper limit (15%). Therefore, Si(IV) cannot replace the Ti(IV) in the [TiO_6] octahedron.

To analyze the elemental distribution in the prepared ceramics, SEM mapping experiments were employed, as shown in Fig. 2. The overlap mapping image in Fig

2b shows a green region corresponding to SiO_2 grains, and a red region corresponding to TINO grains, which was verified by the subsequent EDS images (Fig. 2c–f). Fig. 2c and Fig. 2d clearly show the scattered SiO_2 particles among the TINO grains. However, the In (Fig. 2e) and Nb (Fig. 2f) EDS mapping image was blurry and had weak signals owing to their low doping concentration. Meanwhile, it was observed from Fig. 2c that some of the SiO_2 particles seem to be segregated around TiO_2 grain boundaries, indicating weak or even negligible diffusion between SiO_2 and TINO grains.

HAADF-STEM images were used to confirm that the SiO_2 particles were embedded around the TiO_2 grain boundaries, as shown in Fig. 3. Additionally, it is clear from the line scanning (lower inset of Fig. 3a) and map scanning (upper right inset of Fig. 3a) elemental distribution analysis that the Si(IV) did not diffuse into the TINO grains. This was also verified by the plane-view TEM image (Fig. 3b) of the same region shown in the upper left image in Fig. 3a, and the selected area electron diffraction (SAED) spots for the marked region around the grain boundary (left image in Fig.3b), indicating the good crystalline structure of the TINO and SiO_2 particles. Meanwhile, the SAED spots of regions I, II and III were recorded along the $[\bar{1}11]$, $[\bar{2}22]$ and $[\bar{1}11]$ zone axis, respectively. The lattice planes in each SAED pattern were also given according to the d-spacing of rutile TiO_2 and cristobalite SiO_2.

To observe the surface potentials around the grain boundary[14], scanning Kelvin probe force microscopy (KPFM) was used, as shown in Fig. 4. The top image in Fig. 4 clearly shows a smooth surface with a roughness of less than 20 nm and no notable

variation in the surface, which was a prerequisite for the surface potential test. Under lift mode KPFM the probe was uplifted about 50 nm and a lateral bias of 50 V was applied between the tip of the probe and the surface of the sample, as shown in Fig. 4 middle-lower schematic diagram. Fig. 4 (bottom image) shows that the potential across the SiO_2 band dropped in the plane view and three-dimensional (3D) image, confirming the existence of an electrostatic barrier around the grain boundary, which is thought to be responsible for the lower dielectric loss and high breakdown voltage in the SiO_2–TINO composite ceramics.

Fig. 5 shows the XPS data and fitting lines of Ti 2p (a), Nb 3d (b), Si 2p (c), O 1s (d) and In 3d (e) for the surface of the 2 mol% SiO_2–TINO ceramics. The Ti 2p spectra (Fig. 5a) consisted of well-defined Ti(IV) 2p1/2 and Ti(IV) 2p3/2 photoelectron signals, which were located near 464 and 458 eV, respectively. The spin–orbital splitting between the Ti(IV) 2p peaks was nearly constant at approximately 5.74 eV. The split singlet of O 1s revealed the existence oxygen vacancies.[15] Fig. 5d shows the peak positions of the O1s orbital at 529.9 and 531.1 eV, associated with the Ti–O bond and oxygen vacancy in the rutile TiO_2 structure, respectively. According to the literature,[16] the O1s state always contains a low binding energy peak (LP) and a high binding energy peak (HP) centered at approximately 529.77 and 531.27eV. The LP and HP were attributed to O(II) at the intrinsic sites and the O(II) in the Oxygen deficient regions. The LP and HP were nearly the same strength, indicating that the oxygen existed in oxygen deficient states.

The singlet of Si 2p indicated that only an Si(IV) valence state existed in the sample. No extremely weak low-binding-energy shoulder was apparent for the Nb 3d and In 3d spin–orbit doublet, indicating that they had a single valence state in the specimen. The doublet of Nb 3d and In 3d indicated the existence of Nb(IV) and In(III) in the samples[2a], respectively. It is generally accepted that Nb(IV) is a donor dopant and In(III) is acceptor dopant in the rutile TiO_2 structure.

Fig. 6a shows the dielectric permittivity and loss with respect to frequency for SiO_2–TINO ceramics. It was demonstrated that the TINO ceramics possessed the highest dielectric permittivity and loss. Fig. 6b compares the dielectric permittivity and loss of various ceramics measured at 1 kHz. The dielectric permittivity decreased with increasing SiO_2 up to 6 mol%, and increased slightly at high doping >6 mol%. The dielectric loss decreased drastically from 0.176 to 0.043 with the addition of 2 mol% SiO_2, and then slightly increased to 0.06 with 6 mol% doping; it increased unusually highly when doped with more SiO_2. It should be noted that among these ceramics TINO ceramics doped with 2 mol% SiO_2 possessed the highest dielectric permittivity (33600) and lowest dielectric loss (0.043).

It is noteworthy that the lowest dielectric loss displayed by the 2 mol% SiO_2–TINO ceramic (shown in Fig. 6b) was associated with the highest resistance (15 MΩ) of the grain boundary, as shown in Fig. 7. The impedance spectroscopy (IS) for various compositions was plotted with the real part Z' as the abscissa and imaginary part −Z'' as the ordinate. The Z' and −Z'' of the complex impedance were given as follows:

$$Z' = R_g/[1+(\omega\tau_g)^2] + R_{gb}/[1+(\omega\tau_{gb})^2] \quad (1)$$

$$-Z'' = R_g\omega\tau_g/[1+(\omega\tau_g)^2] + R_{gb}\omega\tau_{gb}/[1+(\omega\tau_{gb})^2], \quad (2)$$

Where R_g and C_g are the resistance and capacitance of the grain (here, corresponding to the TINO main phase), respectively[17]. R_{gb} and C_{gb} are the resistance and capacitance of grain boundary (including the contribution of the SiO_2 particle), respectively. The relaxation times τ_g and τ_{gb} can be calculated by $\tau_g = R_gC_g$ and $\tau_{gb} = R_{gb}C_{gb}$, respectively. ω is the angular frequency, which is equal to $2\pi f$.[17] Fig. S4a and S4b show the enlarged view of the high frequency region, clearly showing the separate grain boundary arc and grain arc in 4 mol% and 8 mol% SiO_2–TINO ceramics. However, the other compositions didn't show the separate grain boundary arc and grain arc, which was thought to be associated with the overlap of two arcs.

Fig. 8 shows the temperature dependence of the dielectric permittivity measured at various frequencies (0.1–1000 kHz) for 2 mol% SiO_2-TINO ceramics. It is clear that the dielectric permittivity decreases with increasing test frequency; although the dielectric permittivity slightly increased with increasing temperature, it also exhibited temperature-independent properties in the range from −55 to 150 °C. It should be noted that the dielectric loss obtained at 1 KHz was below 0.05 over almost the whole temperature range. At high temperatures, both the real and imaginary parts of the permittivity increased at low frequencies, indicating a strong dispersion. This dielectric contribution appeared at 100 °C at 0.1 Hz in all the samples. Such a contribution has often been observed at high temperatures in perovskite ceramics. It was most probably caused by the relaxation of the mobile charge

carriers and had no immediate relation to the present CP phenomena. Therefore, we did not consider this dispersion in the present work.

Fig. 9a shows the current density–electric field characteristics for TINO and 2 mol% SiO_2–TINO ceramics. The HAADF-STEM and KPFM experiments showed that the breakdown voltage of the 2 mol% SiO_2–TINO composite ceramic was much higher than that of the TINO ceramic, which was attributed to the strong blocking effect around the grain boundaries in 2 mol% SiO_2–TINO composite ceramic. Fig. 9b shows the mean and standard errors of the dielectric loss versus frequency between the TINO and 2 mol% SiO_2–TINO composite ceramics (the data was from ten sets of ceramics prepared using the same procedures). Clearly, the 2 mol% SiO_2–TINO composite ceramic had a much lower dielectric loss and fluctuation compared with the TINO ceramics, which was also thought to be associated with the strong blocking effect around the boundaries after doping with SiO_2. As for the TINO ceramic, it was susceptible to the sintering schedule, especially the cooling rate and sintering temperature. In contrast, the dielectric and electrical performance of SiO_2–TINO ceramic was not influenced by the sintering schedule.

Experimental

Materials and methods

The 1 mol% (Nb+In) co-doped TiO_2 (TINO) ceramics were first sintered at 1400 °C for 10 h by standard conventional solid-state method, where the rutile TiO_2 (99.99%), Nb_2O_5 (99.99%) and In_2O_3 (99.99%) powders were used as raw materials. The prepared TINO ceramic was milled to a powder in a ball-milling jar for 4 h in

distilled water with Y-stabilized ZrO_2 media. After drying, the SiO_2 (99.99%) powders were added in stoichiometric proportions (0, 2, 4, 6, 8, 10 mol%). The powders were then re-milled in a ball-milling jar for 2 h in distilled water with Y-stabilized ZrO_2 media. After drying, 5 wt% polyvinyl alcohol (PVA) was added and disks were prepared with a uniaxial press at a pressure of 10 MPa in a stainless steel cylindrical die with a 10 mm diameter. The binder was burned out at 600 °C for 0.5 hours and then the disks were sintered in an alumina crucible at various temperatures (1400 °C, 1450 °C and 1500 °C) and a 3 °C/min heating rate in air for 10 h to obtain dense ceramics. Some samples with a dark blue color resulted from the F-type color center in the rutile TiO_2 structure. Conversely, the milky white region of the sample indicated that the oxygen vacancies generated during the high-temperature-sintering process could not change color.[11,12] The optimum sintering conditions were determined to be at 1500 °C for 10 h. Under these conditions, the highest dielectric permittivity and lowest dielectric loss were achieved. Fig. S1 shows the SEM image for the TINO and SiO_2–TINO composite ceramics.

Characterizations

The phase of the samples was characterized by X-ray diffraction (XRD, D/MAX 2400, Japanese) and Raman spectroscopy (Raman, HR800, France, the 541.32 nm line of Ar^+ laser was used as an excitation source). The microstructure and elemental distribution of the samples were examined by field-emission scanning electron microscopy with energy-dispersive X-ray analysis (FE-SEM/EDX, Quanta F250, USA).

The SiO_2 around the grain boundaries was detected by high-angle annular dark-field scanning transmission electron microscopy (HAADF STEM, TECAI G2F20 FEI, USA), and the elements' distribution was determined on the basis of the Z-contrast image with Z denoting the atomic number. Scanning probe microscopy was conducted using an atomic force microscopy (AFM, Dimension Icon, USA) with a silicon cantilever tip coated with Cr and Co to observe the local potential difference on the polished surfaces. X-ray photoelectron spectroscopy (XPS, AXIS ultra DLD, England) and electron spin resonance (ESR, JES-X330, Japan) experiments were used to analyze the valence state of different elements. The dielectric properties of the ceramics were measured by Agilent E4980A and 4294A with a temperature controller in the range from −150 °C to 200 °C, and a Novocontrol broadband dielectric spectrometer with an Alpha-A high performance frequency analyzer in the frequency range of 10^{-2}–10^{7} Hz over the temperature range of 123–273 K.

Conclusions

The TINO and SiO_2-TINO composite ceramics were synthesized by solid-state sintering methods. The dielectric response of the composite ceramics indicated that the dielectric loss could be lowered to 0.043 while preserving a high dielectric permittivity (~30000), which were not susceptible to change in temperature (−55 to 150 °C) or sintering schedule. Furthermore, the breakdown electric field could be greatly enhanced by doping the TINO ceramics with SiO_2, which were attributed to the strong blocking effect caused by the embedded SiO_2 around the grain

boundaries. From an application viewpoint, further research will concentrate on lowering the sintering temperature and preparing superfine TINO powder.

Notes and references

1 (*a*) X. Cheng, Z. Li and J. Wu, *J. Mater. Chem. A*, 2015, **3**, 5805; (*b*) W. Hu, Y. Liu, R. L. Withers, T. J. Frankcombe, L. Norén, A. Snashall, M. Kitchin, P. Smith, B. Gong, H. Chen, J. Schiemer, F. Brink and J. Wong-Leung, *Nat. Mater.*, 2013, **12**, 821; (*c*) J. Li, F. Li, Y. Zhuang, L. Jin, L. Wang, X. Wei, Z. Xu and S. Zhang, *J. Appl. Phys.*, 2014, **116**, 074105; (*d*) Z. Gai, Z. Cheng, X. Wang, L. Zhao, N. Yin, R. Abah, M. Zhao, F. Hong, Z. Yu and S. Doua, *J. Mater. Chem. C*, 2014, **2**, 6790; (*e*) M. J. Pan and C. A. Randall, *IEEE Electr. Insul. Mag.*, 2010, **26**, 44; (*f*) X. G. Zhao, P.Liu, Y. C.Song, A. P.Zhang, X. M.Chen, J. P.Zhou, *Phys. Chem. Chem. Phys.*, 2015, **17**, 23132; (*g*) J. Li, F. Li, C. Li, G. Yang, Z. Xu and S. Zhang, *Sci. Rep.*, 2015, **5**, 8295.

2 (*a*) J. Li, M. A. Subramanian, H. D. Rosenfeld, C. Y. Jones, B. H. Toby and A. W. Sleight, *Chem. Mater.*, 2004, **16**, 5223; (*b*) C. C. Homes, T. Vogt, S. M. Shapiro, S. Wakimoto and A. P. Ramirez, *Science*, 2001, **293**, 673; (*c*) A. P. Ramirez, M. A. Subramanian, M. Gardel, G. Blumberg, D. Li, T. Vogt and S. M. Shapiro, *Solid State Commun.*, 2000, **115**, 217.

3 (*a*) W. Heywang, *J. Mater. Sci.*, 1971, **6**, 1214; (*b*) M. Fujimoto and W. D. Kingery, *J. Am. Ceram. Soc.*, 1985, **68**, 169; (*c*) B. S. Choiu, S. T. Lin, J. G. Duh and P. H. Chang, *J. Am. Ceram. Soc.*, 1989, **72**, 1967.

4 W. Kobayashi and I. Terasaki, *Appl. Phys. Lett.*, 2005, **87**, 032902.

5 L. Feng, X. Tang, Y. Yan, X. Chen, Z. Jiao and G. Cao, *Phys. Status Solidi A*, 2006, **203**, 22.

6 E. A. Patterson, S. Kwon, C. C. Huang and D. P. Cann, *Appl. Phys. Lett.*, 2005, **87**,

182911.

7 (*a*) L. Liu, Y. Huang, Y. Li, D. Shi, S. Zheng, S. Wu, L. Fang and C. Hu, *J. Mater. Sci.*, 2012, **47**, 2294; (*b*) A. K. Rai, K. D. Mandal, D. Kumar and O. Parkash, *J. Alloy. Compd.*, 2010, **491**, 507.

8 C. Puchmark and G. Rujijanagul, *Nanoscale. Res. Lett.*, 2012, **7**, 1.

9 L. Fang, M. Shen, J. Yang and Z. Li, *J. Phys. D: Appl. Phys.*, 2005, **38**, 4236.

10 M. Li, A. Feteira, D. C. Sinclair and A. R. West, *Appl. Phys. Lett.*, 2006, **88**, 232903.

11 J. Chen, L. B. Lin and F. Q. Jing, *J. Phys. Chem. Solids*, 2001, **62**, 1257.

12 (*a*) J. Li, Y. Pu, Z. Wang and J. Dai, *Ceram. Int.*, 2012, **38**, 6699; (*b*) J. Li, Y. Pu, Z. Wang, Z. Dong and J. Dai, *Mat. Sci. Eng. B-Adv.*, 2013, **178**, 178.

13 A. Kelly and K. M. Knowles, *Crystallography and Crystal Defects*, 2012, 491.

14 S. Y. Chung, I. D. Kim and S. J. L. Kang, *Nat. Mater.*, 2004, **3**, 774.

15 (*a*) B. Erdem, R. A. Hunsicker, G. W. Simmons, E. D. Sudol, V. L. Dimonie and M. S. El-Aasser, *Langmuir*, 2001, **17**, 2664; (*b*) H. Fan, S. Yang, P. Zhang, H. Wei, X. Liu, C. Jiao, Q. Zhu, Y. Chen and Z. Wang, *Chin. Phys. Lett.*, 2007, **24**, 2108.

16 (*a*) T. B. Thiede, H. Parala, K. Reuter, G. Passing, S. Kirchmeyer, J. Hinz, M. Lemberger, A. J. Baucer, D. Barreca, A. Gasparotto and R. A.Fischer, *Chem. Vapor. Depos.*, 2009, **15**, 334; (*b*) M.Fittipaldi, V. Gombac, A. Gasparotto, C. Deiana, G. Adami, D. Barreca, T. Montini, G. Martra, D. Gattechi and P. Fornasiero, *ChemPhysChem*, 2011, **12**, 2221; (*c*) S. P. Harvey, T. O. Mason, Y. Gassenvauser and R. Schafranek, A. Klein, *J. Phys. D: Appl. Phys.*, 2006, **39**, 3959; (*d*) A. Dacca, G. Gemme, L. Mattera and R. Parodi, *Appl. Surf. Sci.*, 1998, **126**, 219-230; (*e*)

Morris, Y. Dou, J. Rebane, C. E. J. Mitchell, R. G. Egdell, D. S. L. Law and M. Casarin, *Phys. Rev. B*, 2000, **61**, 13445; (*f*) B. Erdem, R. A. Hunsicker, G. W. Simmons, E. D. Sudol, V. L. Dimonie and M. S. El-Aasser, *Langmuir*, 2001, **17**, 2664-2669; (*g*) J. Chen, L. B. Lin, and F. Q. Jing, *J. Phys. Chem. Solids*, 2001, **62**, 1257-1262.

17 (*a*) A. R. West, T. B. Adams, F. D. Morrison and D. C. Sinclair, *J. Eur. Ceram. Soc.*, 2004, **24**, 1439; (*b*) J. T. Irvine, D. C. Sinclair and A. R. West, *Adv. Mater.*, 1990, **2**, 132; (*c*) L. Zhang and Z. J. Tang, *Phys. Rev. B*, 2004, **70**, 174306; (*d*) Y. H. Lin, J. Cai, M. Li, C. W. Nan and J. He, *J. Appl. Phys.*, 2008, **103**, 074111.

Figure captions:

Fig. 1 Phase structure of the TINO and SiO_2-TINO composite ceramics.(a) The XRD powder patterns and (b) Calculated lattice parameters.

Fig. 2 Element distribution of the SiO_2-TINO composite ceramic. (a) SEM images for 2 mol% SiO_2-TINO ceramics. (b) The X-ray element (Si, Ti, In, Nb) overlap mapping EDX image. The following EDX images were the respective mapping image of Si (c), Ti (d), In (e) and Nb (f).

Fig.3 SiO_2 segregated around gain boundaries in the SiO_2-TINO composite ceramic.. (a) The left-upper was the HAADF STEM image. (b) Left image was the plane-view TEM image of the same region. Right images were the Selected Area Electron Diffraction (SAED) spots.

Fig.4 Surface potential microscopy of the SiO_2-TINO composite ceramic. Left-upper was the surface topographic image with AFM. Right-upper and Right-lower were the 3D view of surface topographic image and surface potential image, respectively.

Fig. 5 Element valence state of 2 mol% SiO_2-TINO ceramics. Experimental XPS data (open circles) of Ti 2p (a), Nb 3d (b), Si 2p (c), O 1s (d), In 3d (e).

Fig. 6 Dielectric behaviour of TINO and SiO_2-TINO composite ceramics. (a) Dielectric permittivity and loss with respect to frequency. (b) The dielectric permittivity and loss measured at 1 kHz.

Fig.7 Impedance spectroscopy of SiO_2-TINO composite ceramics. The solid symbols were the experimental results. The solid lines corresponding to each solid symbol were the best fitting results according to Eq. (1) and (2).

Fig.8 Temperature dependence of SiO_2-TINO composite ceramics. Dielectric permittivity and loss of 2mol% SiO_2-TINO ceramics in range from -55 to 150 ^{o}C (the temperature range of X8R).

Fig.9 Current density-electric field characteristics and the mean and standard error comparison of TINO and SiO_2-TINO composite ceramics. (a) Current density-electric field characteristics. (b) The mean and standard errors of dielectric loss versus frequency.

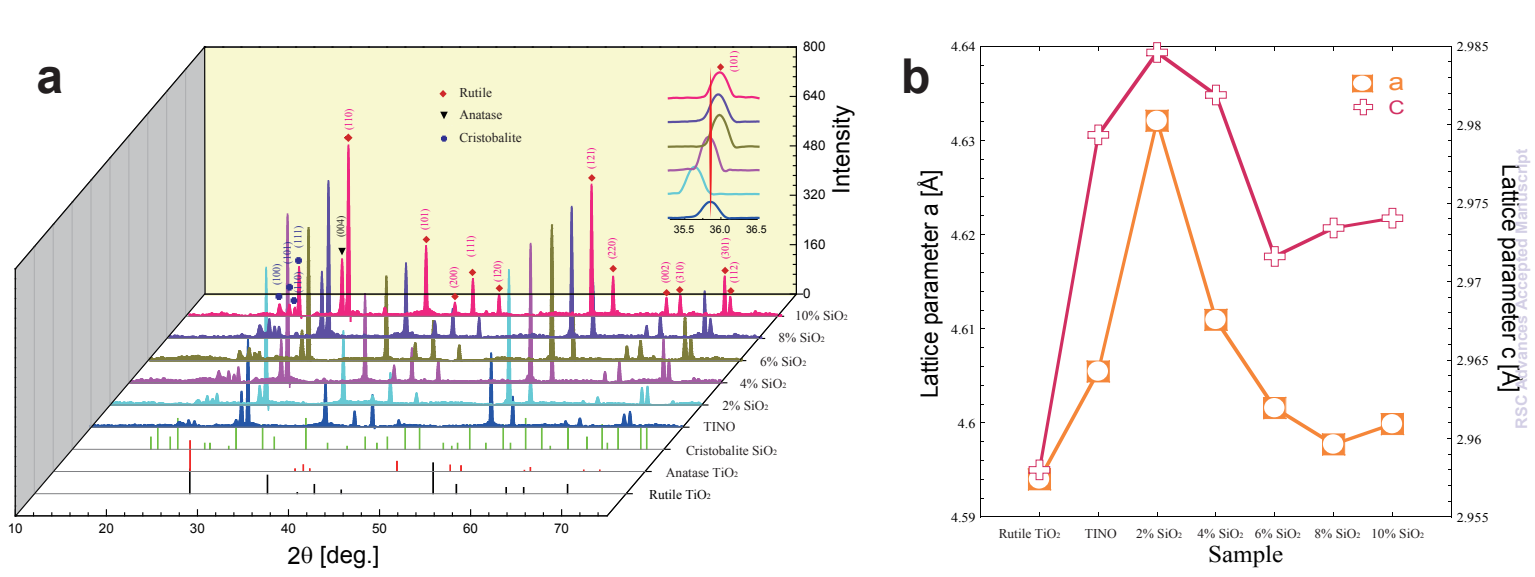

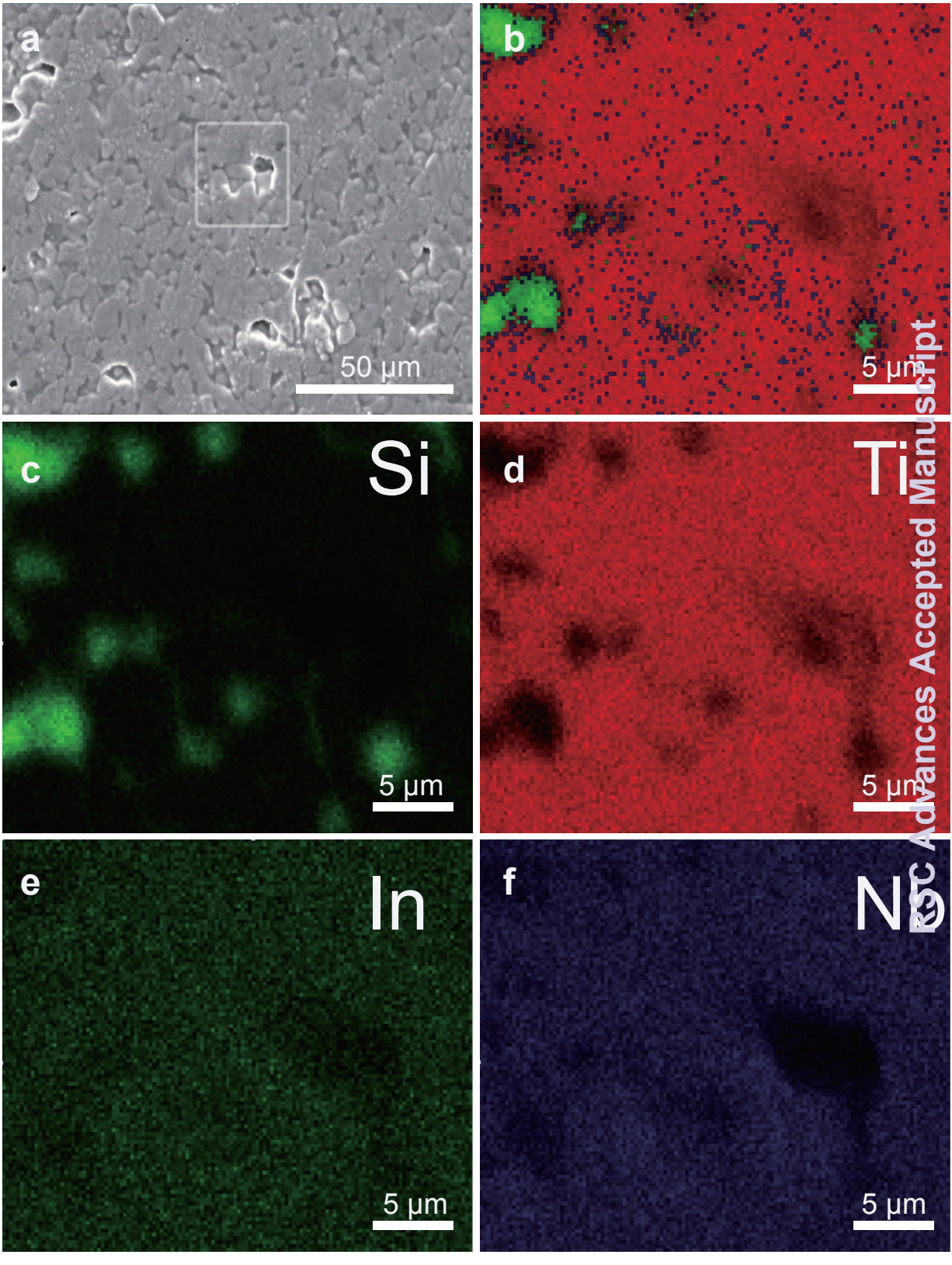

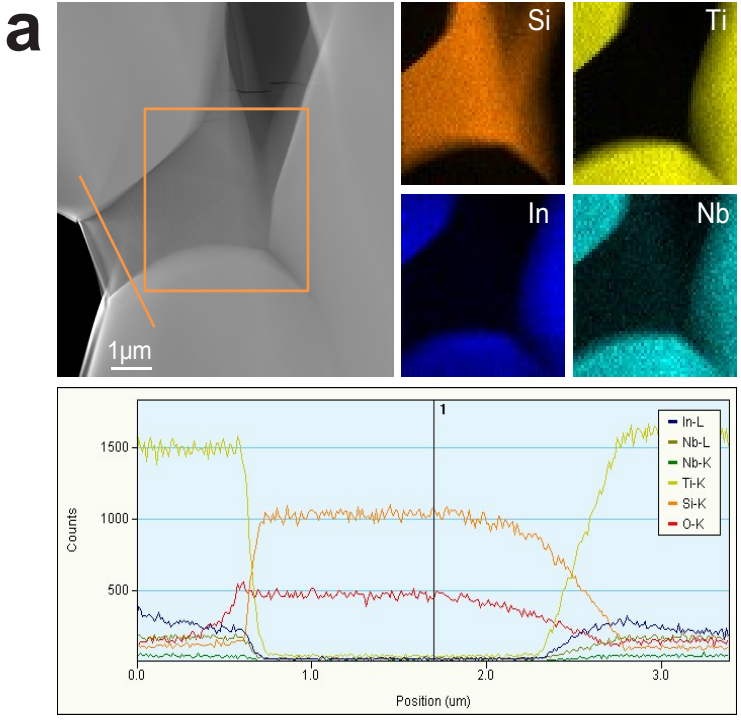

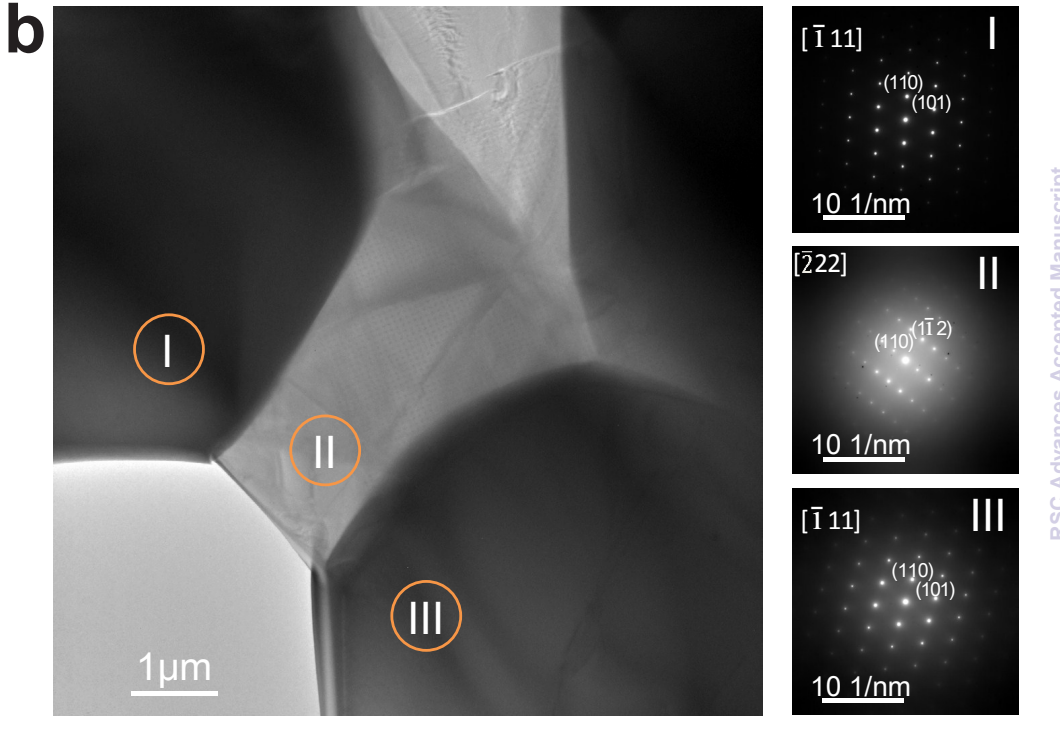

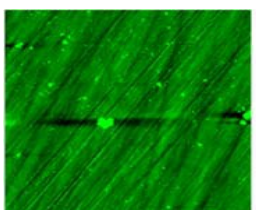

Tapping mode

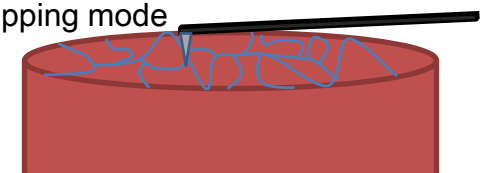

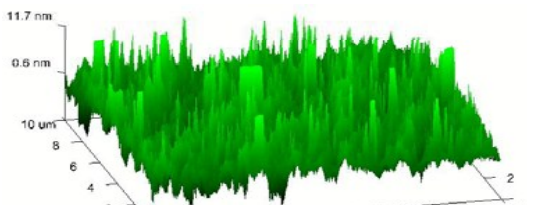

Plan view ⟷ 3D view

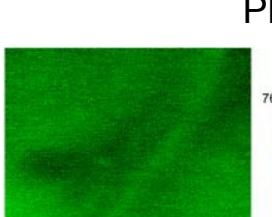

Lift mode